FURTHER DEVELOPMENTS IN PROCESS MAPPING AND MODELLING IN DIRECT METAL SELECTIVE LASER MELTING

C. Hauser, T.H.C. Childs and M. Badrossamay
School Of Mechanical Engineering, University of Leeds, UK

Abstract

This paper advances previous reported work on the mapping and modelling of single tracks and layers produced in powder beds of tool steel and stainless steel powders by a CO_2 laser. For single tracks it reports on predicted and simulated track masses. It validates the simulations, including the use of absorption close to 1.0 when cylindrical tracks are formed. It also reports on melt pool temperature calculations and estimated melt pool dimensions which are used, in conjunction with bed physical properties, to explain why the single tracks form as either continuous with a crescent shape cross-section, continuous with an elliptical section, discontinuously irregularly broken, discontinuously balled or only partially melted as scan speeds and laser powers change. It then extends its scope, experimentally, to consider effects of scan spacing on single layer formation.

Introduction

Metal powders may be processed either indirectly or directly by Selective laser sintering (sls). In the indirect process the laser melts a polymer binder mixed with the metal powder to create a shaped but weak green part. Strengthening occurs from subsequent furnace sintering and infiltration [1]. In the direct process, the laser melts at least a fraction of the metal powder in its path. Traditionally, the powder used is often a specially blended alloy or a powder mixture containing low melting point metal binder particles which braze the non molten structural particles. Component densities are often low and still require strengthening by further sintering, infiltration or hot isostatic pressing [2,3,4]. More recently, a new technique is emerging in which alloy powders and alloy powder blends are totally melted. Its name is selective laser melting (slm), and its aim is to create a strong part that is usable without further processing other than perhaps surface finishing. However, processing is much more difficult by this route and is still the subject of major research studies. Control of melt pool flow is one major issue, more difficult for standard alloys with small melting temperature ranges [5] than for specially developed alloys or powder mixes with a wide range [6]. Frequently, fully molten metal will refreeze as unconnected or loosely connected balls rather than continuous tracks [7,8,9]. There are a number of approaches to avoiding this. Some authors propose as high a scan speed U as possible, subject only to keeping the energy density $P/(U)$ within a certain range, where P is the laser power [7]. Others suggest using low P and U to avoid balling [8,10]. Most successful processing is with special alloys, with parts built up on a substrate, but that limits the areas to which the processing may be applied.

The work of which this paper is part aims to process standard alloys without supports. This paper records the track forms seen in different (P,U) conditions when single tracks of ferrous alloy powders are melted by a continuous wave CO_2 laser, scanning at low speeds. Depending on laser power and scan speed, tracks are formed either fully melted, partially melted or not melted at all. The fully melted tracks are either continuous or balled. An understanding of

what causes which form is then developed. A thermal model which enables the amount of melted powder to be predicted is tested on experiments and used to estimate the temperature field created in and around the melt pool. The model is then briefly applied to the simulation of raster scanning multi-track, single layer coupons, to explore the changes associated with melting powder in close proximity to melted and solidified powder.

The Finite Element Model

The finite element thermal, powder melting and densification model which is used for thermal and post processing calculations is discussed. The methods have been described before, both for laser sintering of polymers [11,12] and for recent developments in quantifying temperature fields created in metal slm [13,14]. It is the continual development of the latter which is the subject of review here.

The calculation is a time stepping one. To start, melted tracks or layers may already exist in a bed. The laser is turned on and the first time step Δt started. A finite element calculation updates the bed temperature $T(K)$ over the time interval Δt. The bed density ρ (or porosity ε) is updated according to a (T,t) densification law. This leads to bed geometry change. The cycle is repeated as often as is required by the specified laser scan pattern. In the temperature calculation, thermal conductivity in the melted material and powder bed is assumed to vary with porosity as observed experimentally for copper [15]:

$$k = k_s (1-\varepsilon)/\left(1+a_k \varepsilon^{0.78}\right) \tag{1}$$

where k_s is the solid conductivity and a_k is chosen to fit the measured initial bed conductivity to its measured initial porosity. k_s and heat capacity C_p are assumed to vary linearly with temperature:

$$k_s = k_{s,o} + a_{k,s} T, \qquad C_p = C_{p,o} + a_C T \quad . \tag{2}$$

Evolution/absorption of latent heat L on melting/solidifying over the solidus/liquidus range T_S to T_L is treated by the temperature recovery method [16]. The move to metal track modelling mainly requires a shift from two to three dimensional modelling. However, some 2D results of metal powder bed melting simulations are reported in this paper. A five hundred-fold reduction in computation time has been achieved by changing the finite element solver from the previously used LUD method to a sparse matrix method [17]. Powder bed density is assumed to change from its initial value to that of solid material as temperature increases from T_S to T_L. Based on viscosity dependence on solid fraction X in mushy state forming [18], it is supposed that there is no densification for $X >> 0.5$ but as X reduces below 0.5, densification increases instantaneously to a value depending on X. An empirical equation with these characteristics is, in terms of porosity:

$$1-\left(\varepsilon/\varepsilon_{powder}\right) = \{\tanh(a_m[1-X])\}^n \tag{3}$$

$a_m = 5$ and $n = 4$ give significant densification for $X < 0.7$ and have been used here. X has been assumed to change linearly from 1 to 0 as T increases from T_S to T_L. The model does not follow convection of material in the melt pool. Densification is assumed to result in sinking of solidified material below the surface of the bed to form a crescent section track. However, total cross-section area and hence mass m per unit length is calculated, as is the equivalent diameter D

supposing the track is cylindrical. Thermal conductivity of and absorptivity α of laser energy into the powder bed are inputs to the thermal model. An approach to determining these, based on theory in [19], is used here. If heat $\alpha P \Delta t$ is instantaneously absorbed at a point on the surface of a powder bed, the maximum temperature rise at a depth z below the surface and the time taken for that to occur are:

$$\Delta T_{\max} = 0.147 \frac{\alpha P \Delta t}{\rho C_p z^3}, \qquad t_{\Delta T \max} = \frac{\rho C_p z^2}{6k} \tag{4}$$

These equations are correct to better than 5% for laser beams of diameter 2a irradiating a surface for the finite time Δt provided $z/a > 4$ and $\Delta t / t_{\Delta T max} < 0.1$. A minimum estimate of absorptivity α_{min} is obtainable from the track melting experiments themselves. Equating heat absorbed to heat needed to melt the track gives:

$$\alpha_{\min}(P/U) = m\{C_p(T_L - T_o) + L\} \tag{5}$$

where T_o is ambient temperature. Consideration of α values is of major importance in this paper.

Experimentation

Materials. Three types of gas atomised powder have been used in this investigation: M2 and H13 standard tool steels and a stainless steel powder which is a high carbon content variant of type 314s that is used for high temperature super plastic forming moulds. The composition of each and their melting data is given in Table 1. All powders were obtained from Osprey Metals Ltd, UK and were supplied with a particle size distribution of -150 + 75μm and -75 + 38μm. No heat treatments, additives or fluxes or powder pre-heating was used in this work.

Equipment. The slm equipment has been described before [13,14]. A 120mm X 150mm tray, which contained the levelled powder bed to a depth of 7mm, was used for all single track and layer tests. The tray was placed within a custom built chamber able to be evacuated to 50mbar gauge pressure then back filled with a process gas to a pressure typically 30-50mbar over atmospheric to minimise leakage into the chamber. Before a series of tests the back filling cycle was repeated twice and the system was left to stabilise for 15mins. During stabilisation and testing, the gas flow rate through the chamber was 3 litres/min. In most of the tests reported here the process gas was 99.9% pure argon, but in one set of conditions melting was carried out in argon to which 10% hydrogen was added.

Melting Experiments. Single tracks and layers have been melted, by a scanning CO_2 laser beam, in the surface of beds made from gas atomised powders of composition and size fraction reported above. Beam diameters at the powder bed surface were 0.6 mm and 1.1 mm. Delivered powers and scan speeds have ranged from 10 to 200 W and 0.5 to 50 mm/s for single tracks and 0.5 to 500mm/s for layers (see Table 2). For the layers the scan spacing's were 0.15mm, 0.3mm and 0.45mm (25%, 50% and 75% of the beam diameter respectively). The tracks were nominally 30mm in length and 7mm apart and the single layers were 15mm x 15mm square. After a test, the tray was removed and the tracks and layers photographed in situ. Those tracks which were continuous and those layers which remained intact when handled were removed from the bed with tweezers, brushed to remove excess powder as best as possible, and weighed. The actual lengths, cross sections and widths and depths of single tracks were measure with callipers.

Simulations. The finite element model was used to simulate in the same conditions as the experiments. The main calculated quantities were the temperature distribution in the powder bed and the mass per unit length of melt tracks. The temperature distribution enabled length, width and depth of the melt pool to be estimated. Two estimates of mass per unit length were calculated, an upper one for which the mass was taken to be of all that powder which experienced an increase in density of more than 100 kg/m^{3}and a lower one which included all material that densified to within 300 kg/m^3 of fully dense. The estimated masses were not sensitive to small changes in these chosen boundary values. The thermo-physical properties of 314S-HC, M2 and H13 in the solid state that were used in the simulations are listed in Table 3. Linear approximations to thermal conductivity and specific heat were obtained from data between about 100°C and 700°C in [20], though it was assumed that the specific heat of M2 was the same as that of H13. T_S and T_L for M2 and H13 were calculated using ThermoCalc^{TM} software and the Scientific Group Thermodata Europe (SGTE) Solid Solution (SSOL) database. Phase diagrams have been published previously [21]. T_S and T_L for 314S-HC were estimated from a conversion of its composition into Ni and Cr equivalents, according to formulae given in [22]. Values for L were obtained from the rule of mixtures and the latent heats of melting of the main alloy components Fe, Cr and Ni (again taking M2 and H13 to have the same values). All the materials were assumed to have a solid density of 7850 kg/m^3. The laser beam was modelled to have a Gaussian distribution of power across its diameter.

Table 1: Powder Composition and Melting Data

Material	Composition, balance Fe							T_S	T_L	L
	C	Si	Cr	Ni	Mo	W	V	(°C)	(°C)	(kJ/kg)
M2	1.0	0.45	4.15	-	5.0	6.4	2	1246	1437	270
H13	0.4	1.0	5.0	-	1.3	-	1	1361	1471	270
314s	0.4	1.0	25	20	-	-	-	1280	1380	280

Table 2: Experimental Conditions.

Experiment	**Laser Power (W)**	**Scan Speed (mm/s)**	**Scan Spacing (mm)**	**Layer Thickness (mm)**
Single tracks	32, 58, 77, 110, 143, 170	0.5, 1 – 12, 15, 18, 20, 25, 30, 35, 40,45, 50	n/a	n/a
Single Layer	32, 58, 77, 110, 143	0.5, 1, 2, 3, 5, 8, 10, 12, 15, 18, 20, 25, 30, 40, 50, 80,100, 120, 150, 200, 250, 300, 400, 500	0.15, 0.3, 0.45	n/a

Table 3: Solid material properties, derived from published sources.

Material	$k_{s,o}$ (W/mK)	$a_{k,s}$ (W/mK^2)	$C_{p,o}$ (J/kgK)	a_c (W/mK^2)
314s	7.8	0.018	437	0.275
M2	18.1	0.011	313	0.5
H13	28.6	0.00	313	0.5

Further Experiments. Measurements of powder bed conductivity and absorptivity of laser radiation have been calculated from the theory based on equations 4 after heating beds with a 4mm diameter stationary 10W CO_2 laser beam for 15s and measuring the variation of temperature with time 10mm below the beds surface, with a copper-constantan thermocouple. Beds were made in a similar manner to the main tests (to obtain similar density), but 30mm deep in a cylindrical container of 60mm internal diameter (the dimensions were tested to be effectively infinite from the point of view of heat conduction over the time period of the experiment). These experiments differed from the main tests in that they were carried out in laboratory air, rather than argon.

Single Track Experimental and Simulated Results

Five different qualitative forms of track were observed in the powder beds. Figure 1 illustrates these with examples formed at powers between 77W and 110W. At the lowest scan speed, in an argon atmosphere, tracks (type A) were continuous and flat-topped or slightly concave in the surface of the powder bed. This is the shape expected from densification by melting, without material re-arrangement by convection or surface tension effects. With increasing speed, tracks (type B) remained continuous but became rounded and sank into the powder bed. This shape change, most likely caused by convection driven fluid motions (see later), causes a large denude area or trench to surround the track. In Figure 1, the rulers next to the type A and B tracks, with their 0.5mm divisions, give a scale to all of the tracks. Each ruler rests on the powder bed and therefore the region of dark shadow between the ruler and the track helps define track shape and gives an indication of the degree of sinking. As the scan speed increases still further, the tracks (type C) became occasionally broken, although not always with the regularity of the example in Figure 1. Each fragment was still cylindrical in shape, and was often formed with a bobble of material at the start and, to a lesser degree, at the end of each melt fragment. The melt fragments were again surrounded by a denude area but did not sink to the same degree as track type B, with the characteristic bobble often rising above the level of the powder bed. At even higher speeds, the tracks became more regularly and frequently broken (type D). The termed 'balled' to describe the tracks became appropriate. Trenching, although to a much lesser degree, was still visible and the majority of the ball volume was sat up above the surface of the powder bed. At the highest speeds, extremely fragile tracks were formed (type E). It will be shown later that these occur in conditions where maximum temperatures exceed T_S but do not reach T_L. They may therefore be described as partially melted.

Process maps were created, to show the combinations of laser power and scan speed at which the different track types formed. Figure 2 shows four examples. In each, the dots mark the P,U combinations at which tests were carried out. The letters A to E show the regions of each track type. The region F is where laser power was insufficient to melt powder. All maps were qualitatively similar. Maps were also created for H13 and 314s -150/+38 powders using a 10% hydrogen addition in the process gas. These maps were again similar and so were deemed unnecessary to be shown here.

Figure 3, shows track cross section shapes to either side of the A-B boundary for H13 -150/+75 powder. The change from flat to rounded tracks at crossing the boundary at constant power is accompanied unexpectedly by an increase in cross section area. This is discussed in detail in [14]. However, for the completeness of results it is important to re-emphasise the changes in calculated laser absorbtivity, α_{min}, (equation 5) from track mass/unit length data as the

A-B boundary is crossed. Values of C_p and L from Table 1 were used. Figure 4 presents the calculated values. The increase in track cross section shown in Figure 4 is associated with an effective increase in absorption. Values greater than 1.0, as shown for M2 are clearly impossible. Perhaps inaccurate values of specific and latent heats have been used, or the tracks contain material that has not fully melted. Nevertheless, values are clearly greater than normally associated with absorption of $C0_2$ laser radiation by metal powders. These expected lower values are confirmed by the results of the further experiments using the stationary laser beam. The results of the further experiments are collected in Table 4. It also summarises the absorbtivity data from mass/unit length calculations, as well as powder bed densities and their thermal conductivities. Figure 4 also shows stills of tracks longitudinal section either side of the A-B boundary. The track nose is rounded. It has been discussed in [14] that that the shape of the leading edge of the track reflects the laser beam forward, creating a region of secondary melting. This was found to occur as speeds approx. greater than 2mm/s and may, in part, account for the increase in mass, and associated increase in absorbance, at the A-B boundary.

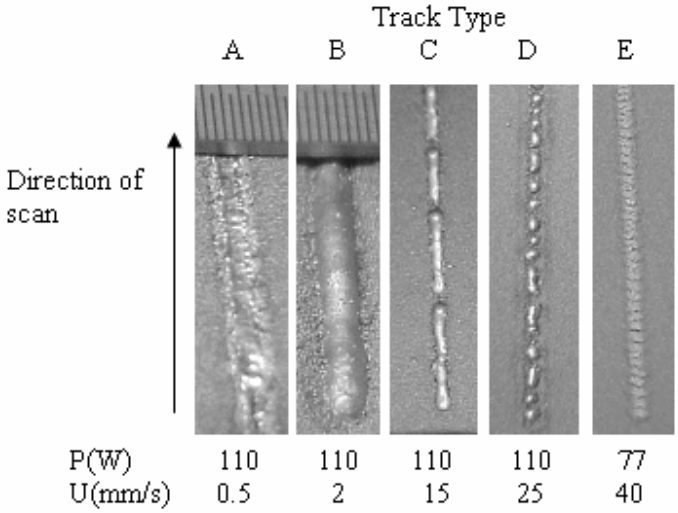

Figure 1: Examples of five types of track A to E (all at nominally same magnification), from tests with -150/+75 μm M2 in argon atmosphere with a 1.1 mm diameter laser beam.

Figures 5 to 8 report example main results of the simulations. Unless otherwise stated, material properties have been taken from Tables 3 and 4. In A and E regions, α values determined from equation 4 have been used, while values from equation 5 have been used in the B, C, and D regions (except that for M2 and H13, α has been rounded to 1.0 rather than using the estimated 0.9 to 1.15 values). Values of a_p (equation 4) have been chosen so that Δz_p is close to the mid-range size of powder particles in a bed (for example, for -150/ +75 μm powders, $a_p = 8$ has been used, giving $\Delta z_p \approx 100$ μm, depending on initial bed density).

Figure 5 compares predicted and simulated track masses. It validates the simulation, including the use of α close to 1.0 when cylindrical tracks are formed. Here the simulations have taken the mass per unit length to include all material densified by more than 10 kg/m^3. Estimates based on almost complete densification are in general 20% to 30% lower (increasing with scan speed).

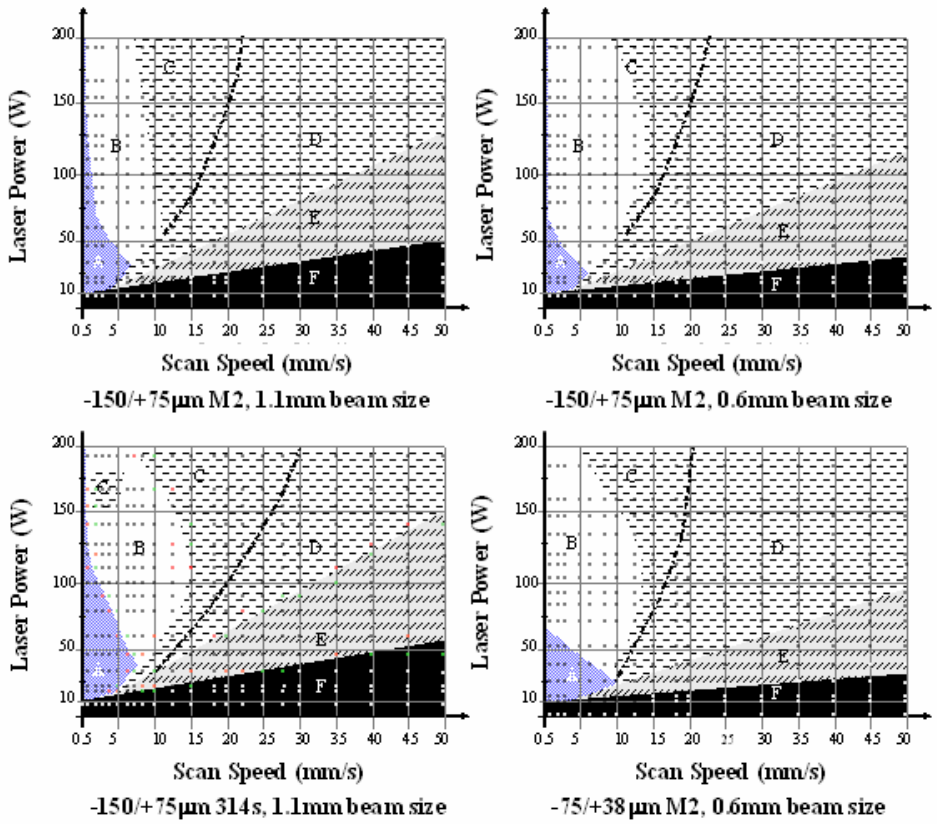

Figure 2: M2, H13 and 314S-HC process map examples, powder size ranges and laser beam diameters as marked.

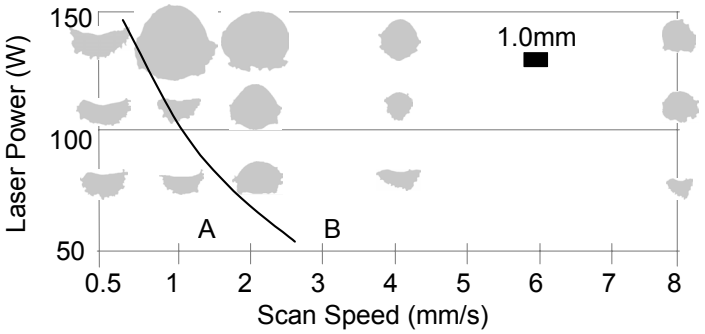

Figure 3: Track cross-sections, H13 steel example

Table 4: Measured powder material properties (-150/+75 µm size fractions except where indicated)

Material	Density ($\rho_{powder\ bed}$)	K (W/mK)	α^1	α^2	
				-150/+75µm	-75/+38µm
314S-HC	4500 ± 30	0.29 ± 0.03	0.28 ± 0.03	0.52 ± 0.05	0.60 ± 0.05
M2	4300 ± 100	0.24 ± 0.03	0.36 ± 0.04	1.15 ± 0.05	not tested
H13	4550 ± 70	0.28 ± 0.03	0.25 ± 0.03	0.9 ± 0.1	1.0 ± 0.1

α^1: from equation (4); α^2 from equation (5)

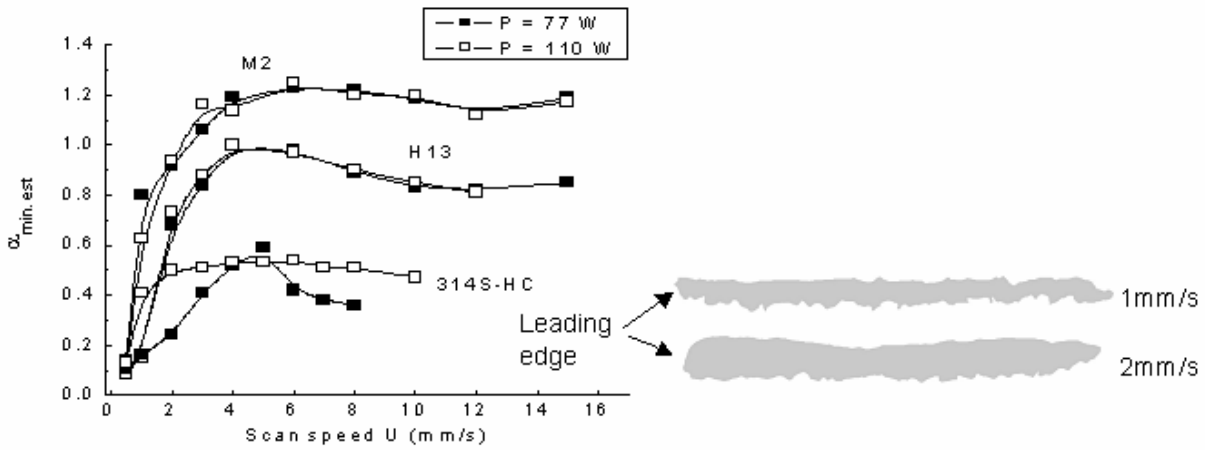

Figure 4 Estimates of α_{min}, for -150/+75 μm powders melted by a 1.1 mm diameter laser beam, with (right) longitudinal track sections for H13 melted at 77W.

Figure 6 investigates temperatures generated in region E conditions for an M2 powder bed example. It centres on a laser power range between 30W and 85W over which type E tracks are formed at a scan speed of 30mm/s. This range is translated from the map onto an adjacent graph which shows the calculated maximum temperature changes of the bed as a function of power, for a scan speed of 30mm/s and α values of 0.36 and 0.25 (0.36 is the value measured for M2 while 0.25 is the lower value measured for H13). The figure supports the hypothesis that the lower limit to region E represents conditions in which peak temperatures just reach T_S while the upper limit corresponds to peak temperatures reaching T_L.

Figure 7 is concerned with conditions around the C-D boundary. Part (a) highlights two paths ab (crossing the C-D boundary at a constant power of 77W) and cd (along the C-D boundary) in the M2 process map. Part b records the calculated time in the melt and the length to diameter (L/D) ratio of the melt pool (assumed cylindrical). Part (b) presents calculated maximum melt time for M2 material in a track and calculated length to diameter ratio of the melt pool, as scan speed is increased along path ab. Melt time reduces from close to 5s at the scan speed of 1 mm/s to 0.16s at the C-D boundary. Over that speed range, the melt pool length reduces from 4.8 mm to 2.4 mm (the melt time is the melt length divided by the scan speed) and the melt pool effective diameter (estimated from the track mass per unit length, on the assumption that the track cross-section is circular) reduces from 2.4 mm to 0.6 mm. As a result the length to diameter ratio increases along ab, reaching the value of 3.1 at the C-D boundary. Part (c) presents length to diameter ratios along the line cb, for M2 as well as the other two materials. The results support the hypothesis that the C-D boundary is one of approximately constant melt length to diameter ratio. The constant lies in the range 2.8 to 3.3.

Figure 8 is concerned with the A-B boundary. Part (a) reproduces a detail of the 314S-HC process map from Figure 2. Simulations have been carried out at constant power and increasing scan speed, along the three dashed paths (P = 77W, 110W and 143W) shown in the figure. Part (b) shows how the surface temperature gradient in the melt varied along these path, assuming the maximum temperature is at the centre of the melt pool (simulated) and the edge of the melt pool was at the temperature T_L. The asterisks mark the conditions at the A-B boundary. A-B may be a boundary of constant melt surface temperature gradient, of around 280 °C /mm to 320 °C/mm.

As the simulations do not model surface tension or convection driven fluid motions, and region A is one in which such motions do not occur, the measure is appropriate for conditions in region A, up to the A-B boundary.

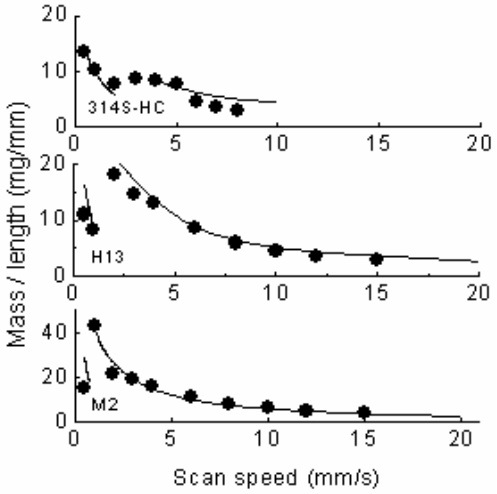

Figure 5: Experiment (•) and simulation (—), P = 77W

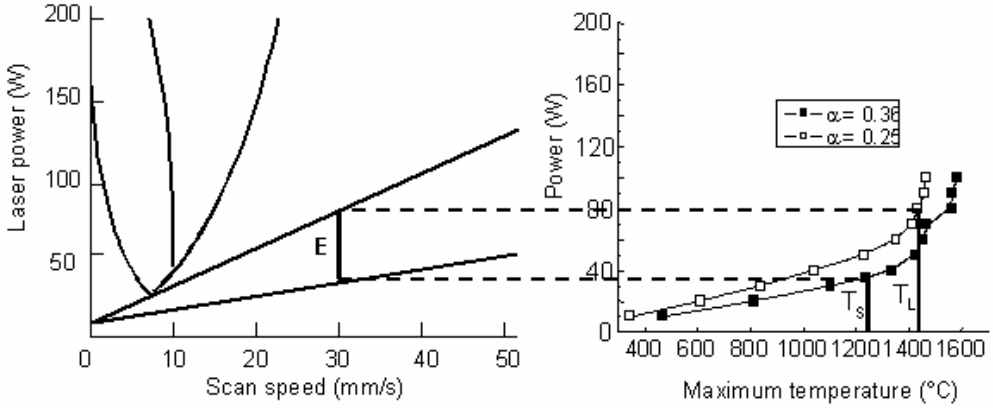

Figure 6: Process map for M2, -150/+75 μm powder size and 1.1 mm laser beam diameter, with temperature calculations at a scan speed of 30 mm/s

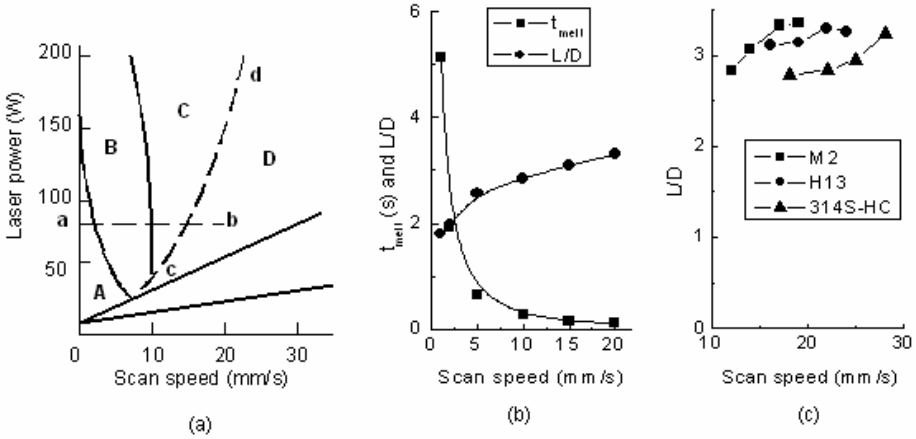

Figure 7: (a) Part of M2 process map as Fig 10; (b) calculated t_{melt} and L/D along line ab; (c) L/D along line cd (also with values for 314S-HC and H13)

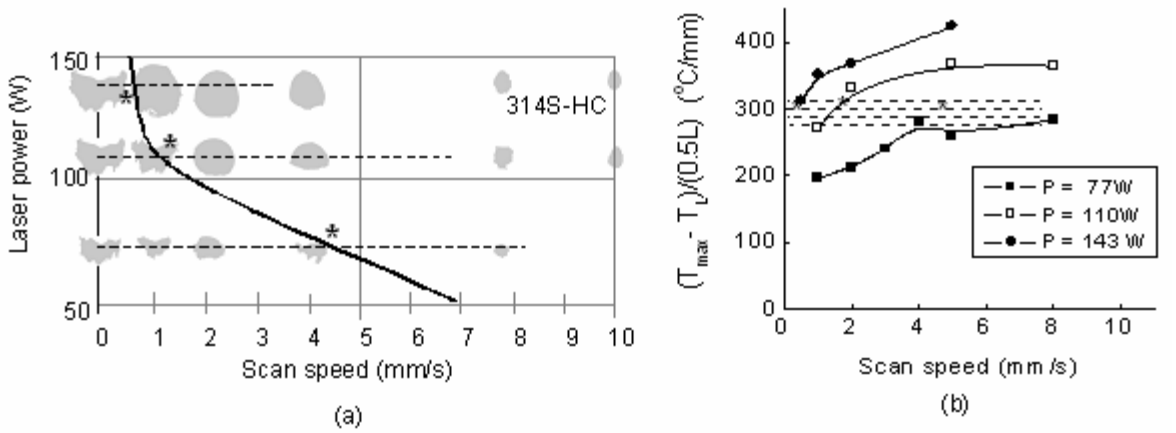

Figure 8: (a) A-B region process map for 314S-HC from Fig 6; (b) surface temperature gradient calculations along the dashed-lines of part (a)

Single Layer Results

Three different qualitative forms of track were observed in H13 powder beds (-150/+75μm). Figure 9 illustrates these with example layers formed at powers between 58W and 143W and for scan spacing's of 0.15mm and 0.45mm. The processing gas was argon. At scan speeds below 150W (actual value dependant on laser power) layers (type 1) were fully melted with no to very little porosity. The porosity level was observed by holding the sample layer in front of a light box. With increasing speed, layers (type 2) were still fully melted but contained a much higher level of porosity (the actual level increased with increasing speed). Porosity levels were not measured but were judged to range between 60% and 95% of theoretical density. As the scan speed increased still further and as the laser power began to reduce, the layers (type 3) became very fragile and extremely porous, to a level where their removal from the powder bed became impossible without breakage.

Process maps were created, to show the combinations of laser power and scan speed at which the different layer types formed for scan spacing's of 0.15mm and 0.45mm (Figure 10a/b). Region 4 is where P/Us values were insufficient to melt the powder. A further two maps were also created (Figures 10c/d) which superimpose, for both scan spacing's, layer types 2 then 3 with track types C then E respectively. These groupings were chosen due to their close boundary proximity's over the scanning conditions investigated, suggesting that perhaps porosity within a layer occurs due to the break up of the individual tracks.

Conclusions

Five different track forms have been identified, depending on laser power and scan speed In region A, the tracks have a flat or slightly crescent shaped surface. The longitudinal track sections (Figure 4) suggest that the melt wets the surrounding powder. The melt ceases to wet the powder at the A-B boundary. This leads to a rise in laser power absorption, a growth of track section and the track sinking into the bed. In region C, tracks are occasionally broken. Even in B, breaks are sometimes seen, caused by interruption of the formation cycle. We suppose that in C, with its short melt times this happens more often. True instability starts at the C-D boundary. *L/D* ratios there are close to the value π expected of a Rayleigh instability. This further indicates that

the melt does not wet adjacent powder in regions B, C, D. In region E, bounded by lines of constant *P/U*, partially melted track is evidence that maximum temperature lies between T_S and T_L.

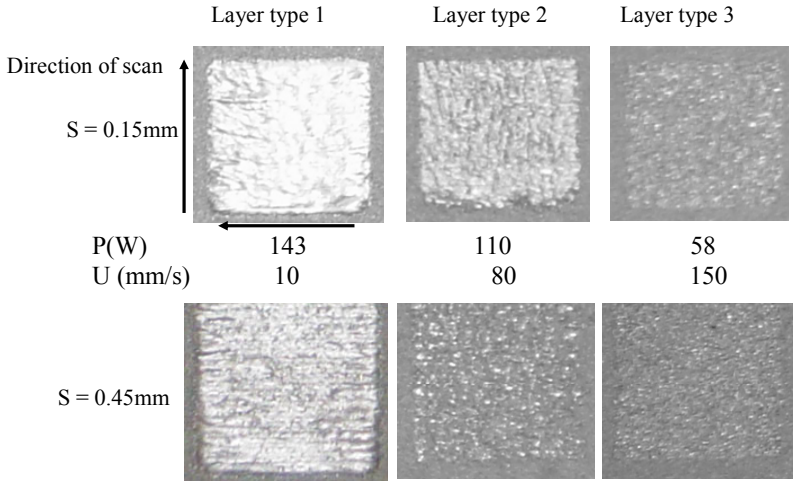

Figure 9: Examples of three types of layers 1 to 4 (all at nominally same magnification) from tests with -150/+75 μm H13 in argon atmosphere with a 0.55 mm diameter laser beam.

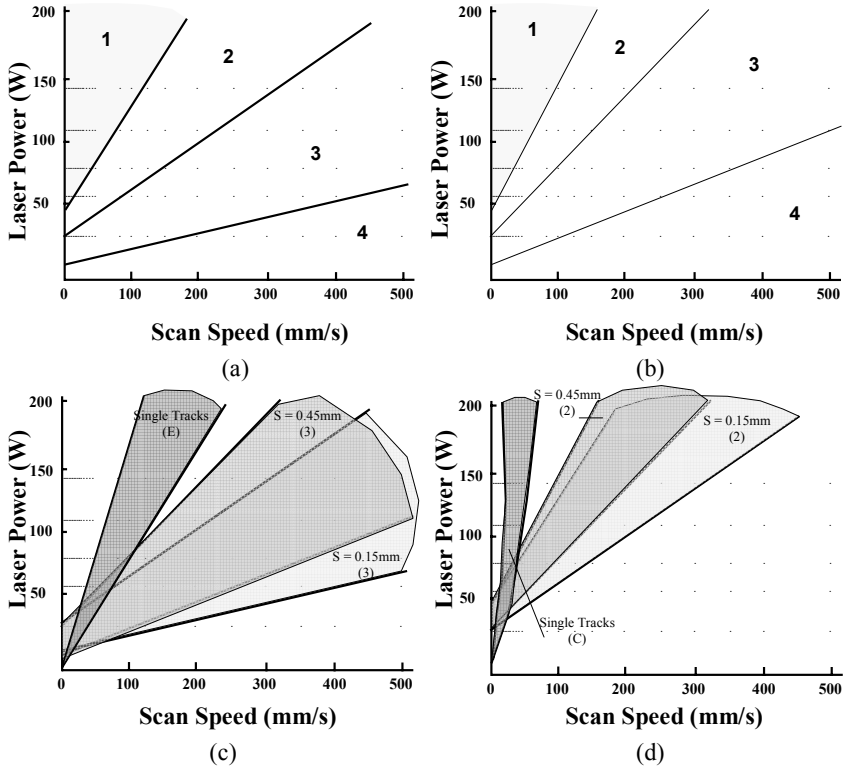

Figure 10: a/b H13 process maps for single layers with scan spacing's of 0.15mm and 0.45mm respectively and c/d track types C and E superimposed onto layers types 2 and 3.

References

[1] K.W. Dalgarno and T.D. Stewart (2001). Manufacture of production injection mould tooling incorporating conformal cooling channels via indirect selective laser sintering. *Proc. Instn. Mech. Engrs., Part B: J. Engineering Manufacture*, 215B, pp.1323-1332.J.P.

[2] J.P. Kruth, X. Wang, T. Laoui and L. Froyen (2003). Lasers and materials in selective laser sintering. *Assembly Automation Journal*, Volume23, Number 4, pp.357–371.

[3] J.P. Kruth, M.C. Lue and T. Nakagawa (1998). Progress in additive manufacturing and rapid prototyping. *Annals of CIRP*, Vol. 47/2. pp. 525-540.

[4] S. Das, M. Wohlert, J.J Beaman and D.L. Bourell (1997). Direct selective laser sintering of high performance metals for containerless HIP. *Advances in Powder Metallurgy and Particulate Materials*, Volume 3, Part 21. pp. 67-78.

[5] H.J. Niu and I.T.H Chang (1998). Liquid phase sintering of M3/2 high speed steel by selective laser sintering. *Scripta Materialia*, 1998, 39, 67-72.

[6] J.P. Kruth, L. Froyen, M. Rombouts, J. Van Vaerenbergh, P. Mercelis (2003), New Ferro Powder for Selective Laser Sintering of Dense Parts, *Annals of the CIRP*, 52/1:139-142.

[7] J.P. Kruth, L. Froyen, J. Van Vaerenbergh, P. Mercelis, M. Rombouts and B. Lauwers, (2004). Selective laser melting of iron-based powder. *Journal of Materials Processing Technology149*. pp.616-622.

[8] F. Klocke and C. Wagner (2003). Coalescence behaviour of two metallic particles as base mechanism of selective laser sintering. *Annals of the CIRP*, 52/1, 177-184.

[9] F. Abe, K. Osakada, M. Shiomi, K. Uematsu and M. Matsumoto (2001). The manufacturing of hard tools from metallic powders be selective laser melting. *Journal of Materials Processing Technology*, 111, pp.210-213.

[10] H.J. Niu, T.H. Chang (1999). Instability of scan tracks of selective laser sintering of high speed steel powder, *Scripta Materialia*. 41 (11) pp.1229–1234.

[11] T. H. C. Childs, M. Berzins, G. R. Ryder, A. Tontowi (1999). Selective laser sintering of an amorphous polymer - simulations and experiments. *Proc. I. Mech. E.* 213B, 333-349.

[12] T. H. C. Childs, A. E. Tontowi (2001). Selective laser sintering of a crystalline and a glass-filled crystalline polymer: experiments and simulations. *Proc. I.Mech.E.* 215B, 1481-1495.

[13] C. M. Taylor, T. H. C. Childs (2002). Morphology of Direct SLS-processed stainless steel layers. *Proc.13th Solid Freeform Fabrication Symposium*, University of Texas, Austin.

[14] C. Hauser et al. (2003). Direct Selective Laser Sintering of Tool Steel Powders to High Density. Part A: Effects of Laser Beam Width and Scan Strategy. . *Proc.14th Solid Freeform Fabrication Symposium*, University of Texas, Austin.

[15] M. Shiomi, A. Yoshidomi, F. Abe and K. Osakada, (1999). Finite Element Analysis of Melting and Solidifying Processes in Laser Rapid Prototyping of Metallic Powders, *International Journal of Machine Tools and Manufacture*, 39:237-252.

[16] T.C. Tszeng, Y.T. Im, S. Kobayashi (1989). Thermal Analysis of Solidification by the Temperature Recovery Method, *International Journal of Machine Tools and Manufacture*, 29:107-120.

[17] Y. Saad and M.H. Schultz, (1985). Conjugate Gradient-Like Algorithms for Solving Nonsymmetric Linear Systems, *Mathematics of Computation*, 44:417-424.

[18] M.C. Flemings (1991). Behaviour of Metal Alloys in the Semi-Solid State, *Metallurgical Transactions*, 22B:269-293.

[19] H.S. Carslaw and J.C. Jaeger (1959). Conduction of Heat in Solids 2nd. ed., *Clarendon Press*, Oxford.

[20] *ASM Metals Handbook 10th edn.*, 1990, ASM, Ohio

[21] S.P. Akhtar, C.S. Wright et al. (2003). Effects of laser beam width and scan strategy during selective laser sintering of tool steel powders to high density: Part B – the effect on microstructural evolution. *Proc.14th Solid Freeform Fabrication Symposium*, University of Texas, Austin.

[22] Anon, *A Guide to the Solidification of Steels*, 1977, Jernkontoret, Stockholm.